minerals

MDPI

Article

Geochemistry, Geochronology, and Hf-S-Pb Isotopes of the Akechukesai Ⅳ Mafic-Ultramafic Complex, Western China

Jiaming Yan [1], Fengyue Sun [1,*], Ye Qian [1,*], Liang Li [2], Yongsheng Zhang [4] and Zhengping Yan [1,3]

[1] College of Earth Sciences, Jilin University, Changchun 130061, China; WL190a@163.com (J.Y.); yzp1235220@163.com (Z.Y.)
[2] School of Resource Environment and Earth Science, Yunnan University, Kunming 650500, China; liliang19@ynu.edu.cn
[3] Qinghai provincial Bureau of Ferrous Metal and Geological Exploration, Xining 810007, China
[4] National Gemological Training Center, Beijing101300, China; 15143032450@163.com
* Correspondence: yjm19910219@163.com (F.S.); qianye@jlu.edu.cn (Y.Q.); Tel.: +86-186-2662-3761

Received: 13 March 2019; Accepted: 01 May 2019; Published: 2 May 2019

Abstract: The Akechukesai Ⅳ mafic–ultramafic complex, located in the western segment of the eastern Kunlun orogenic belt (EKOB), represents a newly-discovered complex, containing Ni ores at grades of up to 0.98% Ni. It is dominated by olivine pyroxenite, pyroxenite, and gabbro units. The gabbros are enriched in lithophile elements (e.g., Rb, U, and K) and light rare-earth elements (LREE), with negative anomalies in high field-strength elements, except Zr, Ta. Nb/Ta(~5) and Zr/Hf (~10) ratios lower than the primitive mantle and chondrites, respectively, indicate the influence of the mantle metasomatic process or fractionation of accessory mineral phases. Zircon U–Pb dating of the gabbro yielded an age of 423.9 ± 2.6 Ma, indicating that the complex formed contemporaneously with the Xiarihamu Ni deposit (423 ± 1 Ma). The gabbro has negative εHf(t) values (–11.3 to –1.2) with corresponding T_{DM1} ages of 1535–1092 Ma. The vein-like and disseminated mineralization (i.e. pyrite and pyrrhotite) have $\delta^{34}S$ values of 13.1‰–13.4‰ and 5.0‰–8.5‰, respectively, suggesting that the magmas that formed the complex assimilated crustal sulfur. They yield $^{206}Pb/^{204}Pb$, $^{207}Pb/^{204}Pb$, and $^{208}Pb/^{204}Pb$ values of 17.323–18.472, 15.422–15.626, and 37.610–38.327, respectively, indicating Pb derived from multiple sources (i.e. mantle crustal sources). Geochemical and Hf–S–Pb isotopic characteristics suggest that the complex formed from a primitive magma derived by partial melting of a spinel- and garnet-bearing lherzolite mantle at variable degree of 5%–10%. This source region was geochemically enriched by previous interaction with slab-related fluids. Tectonic reconstruction suggests that the Akechukesai Ⅳ complex was generated in a post-collisional extensional environment.

Keywords: Akechukesai Ⅳ mafic–ultramafic complex; Hf–S–Pb isotopes; spinel and garnet lherzolite mantle; enriched primitive magma; post-collisional tectonic environment; eastern Kunlun orogenic belt (EKOB)

1. Introduction

The eastern Kunlun orogenic belt (EKOB) is located along the northern margin of the Tibetan Plateau in western China [1] (Figure 1a):

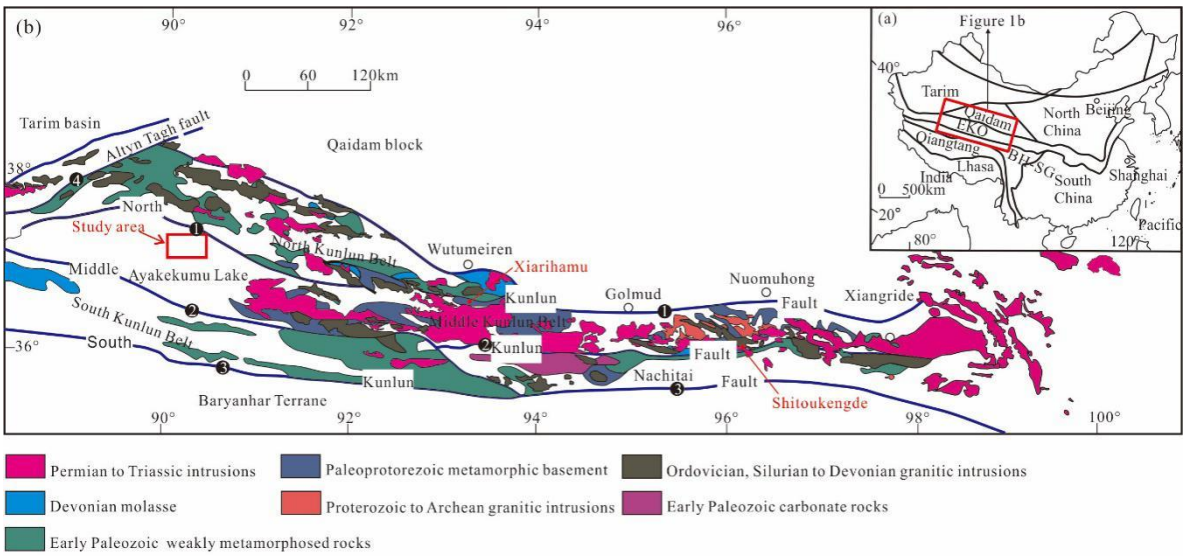

Figure 1. (a) Tectonic sketch map of China (revised after Yuan et al. [2]); (b) schematic geological map of the Eastern Kunlun Orogen (simplified after Xu et al. [3]). ❶-North Kunlun fault; ❷-Middle Kunlun fault; ❸-South Kunlun fault; ❹-Altyn Tagh fault.

Previous researches determined that the orogenic events are associated with the subduction of the proto- and paleo-Tethyan oceans [4,5]. This Silurian–Devonian tectonism also generated widespread magmatic rocks, including granites of slightly variable ages and minor amounts of mafic–ultramafic intrusions [6–9]. The origin of the latter remain poorly investigated despite the fact that some of them are mineralized. For instance, Xiarihamu intrusion contains 1.07 million tons of Ni reserves [7].

The Akechukesai Ⅳ mafic–ultramafic complex was first discovered by researchers from the Jilin University during a geological mapping in the western segment of the EKOB in 2015 (Figure 1b). It is similar to the previously discovered Akechukesai Ⅰ and Xiarihamu mafic–ultramafic complexes in terms of petrological features and metallic mineral assemblage [unpublished data]. The Xiarihamu deposit, one of the largest and best-known magmatic Ni–Cu deposits in this region [6,10,11], was the first Ni–Cu deposit discovered in the EKOB, and formed between late Silurian and Early Devonian (424–406 Ma) [6,7,11]. The discovery of this deposit stimulated more interest in evaluating the potential of the Cu–Ni mineralization in this region. One of the successful activities is the discovery of four mineralized mafic-ultramafic intrusions in the Akechukesai district. On the basis of the analysis of experimental results [unpublished data], these complexes, including the recently -discovered complex IV, could potentially host significant amounts of sulfide ores. Here, we present new geochronological, geochemical, and Hf–S–Pb isotopic data in order to understand its genesis. It provides an excellent example of regional mineralization. The results can contribute to the understanding of mafic-ultramafic intrusion related Cu-Ni deposit.

2. Geological Setting

The EKOB is an important area of the Tibetan Plateau, testifying to an extensive magmatic activity in the western China, and covers an area of ~1000 km^2 (Figure 1b). It contains three major fault zones, namely the North and Middle Kunlun faults and the South Kunlun–Anyemaqen fault. These three fault zones tectonically split the EKOB into three sub-tectonic units, namely the North Kunlun belt, the Middle Kunlun belt, and the South Kunlun belt [12].

The North Kunlun belt is dominated by the Paleoproterozoic–Mesoproterozoic Jinshuikou Group gneiss and the Ordovician–Silurian Tanjianshan Group marble [12,13]. It also contains voluminous high-K calc-alkaline granites [12]. The Middle Kunlun belt is an extensively exhumed belt that contains granitoid units, the Jinshuikou Group as well as small amounts of mafic–ultramafic intrusions. The South Kunlun belt is well-preserved and is dominated by Proterozoic to Triassic units

as well as rare Paleozoic and Mesozoic granitic rocks. These units include the Mesoproterozoic Wanbaogou Group, thought to represent part of an oceanic basalt plateau [12].

The Akechukesai Ⅳ mafic–ultramafic complex is located in the Middle Kunlun belt adjacent to the North Kunlun fault (Figure 1b). Unlike the Xiarihamu and Shitoukengde deposits, the area that hosts the complex contains numerous outcrops of the Tanjianshan Group, whereas the Jinshuikou Group outcrops only within the northeastern part of the district. The structure is dominated by NW–SE trending faults, especially in the northeast of the region. The intrusive units in this area are dominated by four mafic–ultramafic complexes in the form of small intrusive bodies.

3. Geology of the Akechukesai Ⅳ Complex

The Akechukesai mafic–ultramafic complex is divided into four complexes numbered Ⅰ, Ⅱ, Ⅲ, and Ⅳ (Figure 2), all hosting Ni mineralization. The Akechukesai I mafic–ultramafic complex was the first to be discovered, and zircon U-Pb dating suggests it was formed at 422 ± 10 Ma (unpublished data). This research focuses on the Akechukesai Ⅳ mafic–ultramafic complex, which outcrops over an area of approximately 0.1 km^2 and is hosted by marbles of the Tanjianshan Group. It contains olivine pyroxenite, pyroxenite and gabbro units in an increasing order of volume.

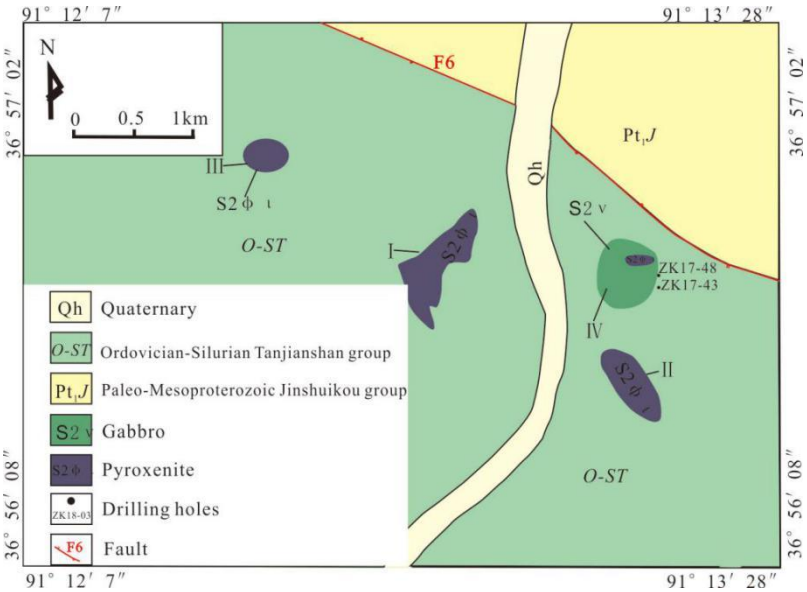

Figure 2. Geological sketch map of the Akechukesai ore district.

Recent explorations (ZK17-43 and ZK17-48 drillholes) intercepted two orebodies with thickness of 51m and 57m and average grades of 0.98% and 0.97% Ni, respectively. Other drillholes in the area also revealed Ni ores. The Ni mineralization identified to date is primarily hosted by pyroxenite units, although Cu of cutoff grades were also identified within several drillholes in pyroxenites. Overall, the Akechukesai Ⅳ appears to be the most economically prospective complex in this region, as a result of the high Ni grades.

The Akechukesai Ⅳ has undergone post-magmatic chlorite hydrothermal alteration. Sulphides within the complex are dominated by pentlandite and pyrrhotite with minor chalcopyrite. The ore minerals in the complex have idiomorphic–hypidiomorphic and inequigranular textures (Figure 3a, b). The sulphides are hosted by vein-like structures and are also disseminated in host rocks; crustal contamination-related evidence of interaction between the magmas that formed the contaminated rocks and the surrounding marble is ubiquitous in the field and cores (Figure 3c–f). Gabbro samples were used for geochemical, geochronological, and Hf isotopic analysis during this study. These gabbros are charcoal grey, massive, medium- to fine-grained, and contain plagioclase (~50% in volume), clinopyroxene (~25% in volume), amphibole (~10% in volume), and biotite (~10% in volume)

with minor amounts of chlorite (~5% in volume). The plagioclase commonly has polysynthetic twins and the pyroxene is partially altered by chlorite (Figure 4a–d).

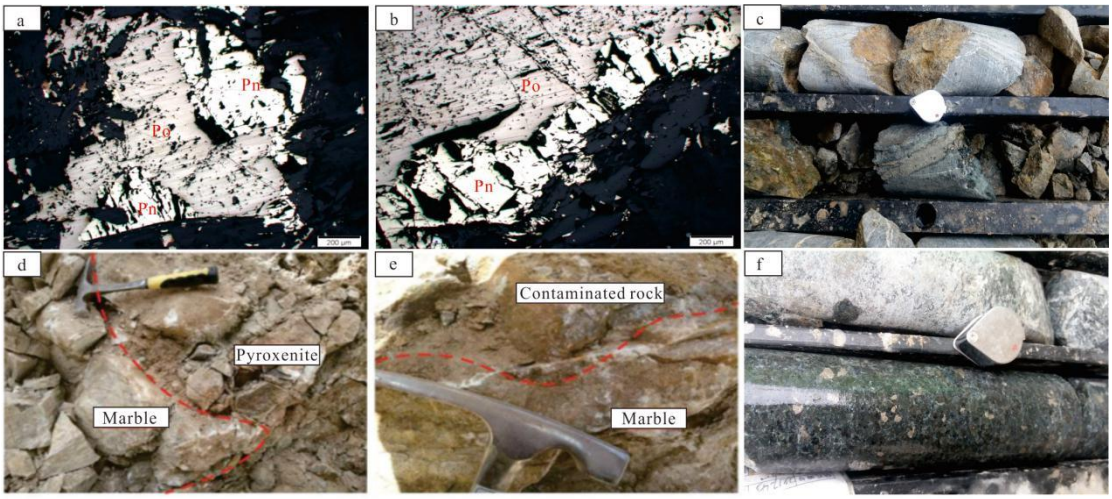

Figure 3. (**a**) (**b**) Microphotographs of ore samples in Akechukesai Ⅳ mafic–ultramafic complex; (**c**) (**d**) (**e**) (**f**) Field and core photos of Akechukesai Ⅳ mafic–ultramafic complex. Abbreviations: Pn = Pentlandite, Po = Pyrrhotite.

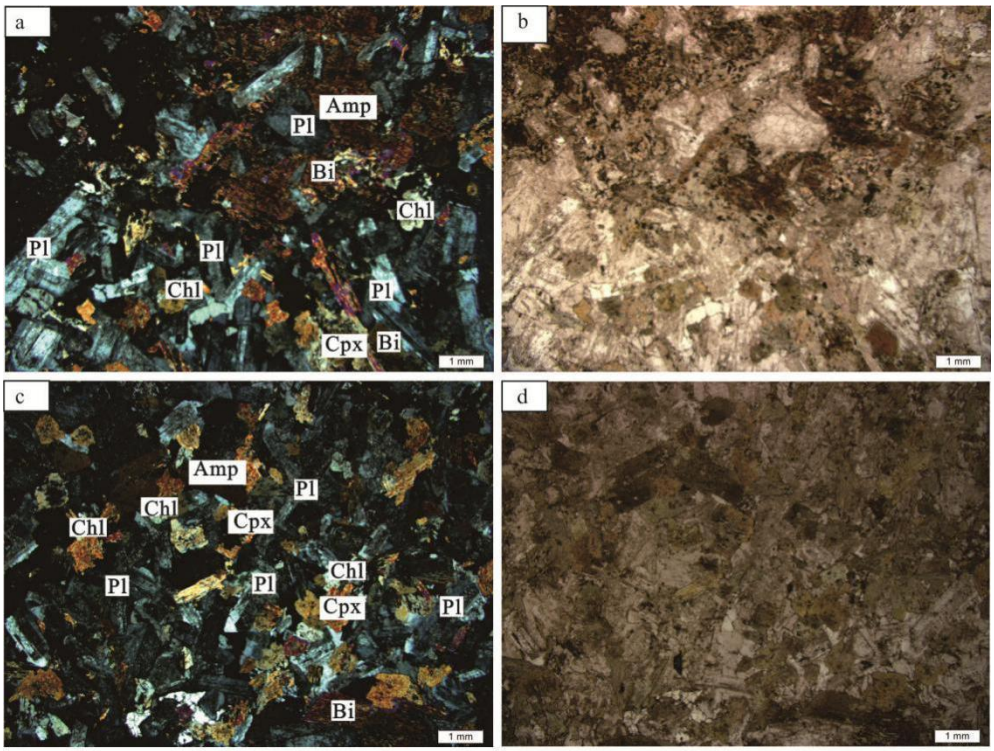

Figure 4. Microphotographs of gabbro samples in Akechukesai Ⅳ mafic–ultramafic complex. Mineral code: Cpx = clinopyroxene, Pl = plagioclase, Amp = amphibole, Bi = biotite. a and c:crossed polars; b and d:parallel polars.

4. Analytical Methods

For gabbro whole-rock samples, altered surfaces were removed before being crushed to ~200 mesh. X-ray fluorescence (XRF; pw1401/10) equipped with ICP-MS (Agilent 7500a) and fused-glass disks were utilized to determine the major and trace element compositions (including Fe_2O_3T content), after digestion of samples in Teflon bombs by HF-HNO_3. The analysis was performed at the testing center of Jilin University, Changchun, China. Standard samples for analysis were AGV-1

(andesite), BCR-2 (basalt), and BHVO-1 (basalt), which indicated that the precision of whole-rock samples was better than 5%. For the determination of FeO content, we used the Potassium dichromate volumetric method. This method follows the standards of GB/T 14505 and GB/T 14506.1 of the People's Republic of China.

The separation process of zircons from gabbros used for U-Pb dating conforms to standard at the regional geology survey, Langfang city, China. Then, transmitted, reflected light and cathodoluminescence (CL) images were obtained to uncover their internal characteristics.

U-Pb dating was performed at the Yanduzhongshi testing company, Beijing, China. The experimental apparatus used was an Aurora M90 ICP-MS interfaced with a New Wave UP213 laser ablation system. Helium and argon served as the carrier and make-up gas, respectively. They needed to be mixed evenly before entering the ICP. The spot diameter for analysis was 30 μm. In order to standardize the instrument, zircon 91,500 and Nist 610 were selected. The detailed procedure and method for common Pb correction are from Yuan et al. [14] and Andersen [15]. Isotopic data and age calculations were performed by ICP-MS, following Liu et al. [16] and Ludwig [17].

In situ zircon Hf isotope analyses were implemented using a Neptune multi-collector ICP-MS equipped with a NewWave UP213 laser-ablation system, at the Chinese Academy of Geological Sciences, Beijing, China. Hf isotopic measurements were done on the same spots previously analyzed for U-Pb with laser spot 30 μm in diameter, repetition rates of 8 Hz, laser beam energy density of 16 J/cm^2, and an ablation time of 31s. Zircons 91,500 and GJ-1 were used to optimize the analytical instruments. The present-day chondritic ratios of $^{176}Hf/^{177}Hf$ = 0.282772 and $^{176}Lu/^{177}Hf$ = 0.0332 were adopted to calculate εHf(t) values [18]. In the calculation of Hf model ages, $^{176}Lu/^{177}Hf$ and $1^{76}Hf/^{177}Hf$ were 0.282772 and 0.28325, respectively [18]. Wu et al. [19] and Guo et al. [20] have previously discussed the laboratory apparatus, testing process, and data capturing process.

Nine sulphides (i.e. pyrite and pyrrhotite) were obtained from the vein-like and disseminated ores for S and Pb isotope analyses, which were done at the test center of Beijing Research Institute of Uranium Geology. A Finnigan MAT 251 mass spectrometer was utilized to analyze the S isotopic compositions and uncertainty was ±0.2‰ for $\delta^{34}S_{V\text{-}CDT}$. The reported data are relative to Vienna Canon Diablo Troilite (V-CDT) sulfide. As for Pb-isotopic compositions of sulfides, 50 mg of powder was dissolved in a mixed solution of hydrofluoric and perchloric acid, followed by elution through anion exchange resin, to separate Pb. The Pb isotopic compositions were measured on an ISOPROBE-T Thermal Ionization Mass Spectrometer with the standard NBS SRM 981. The precisions for $^{204}Pb/^{206}Pb$ and $^{208}Pb/^{206}Pb$ ratios were better than 0.005.

5. Analytical Results

5.1. Major- and Trace-Element Compositions

The major- and trace-element compositions of the samples analyzed during this study are given in Table 1. The samples have generally uniform compositions and contain 53.20 wt.%–53.75 wt.% SiO_2, 6.15 wt.%–6.31 wt.% MgO, 17.88 wt.%–18.25 wt.% Al_2O_3, 0.99 wt.%–2.17 wt.% Fe_2O_3, 7.86 wt.%–9.01 wt.% CaO, and 0.67 wt.%–0.80 wt.% TiO_2. They have $Mg^{\#}$ (= $100*Mg^{2+}/(Mg^{2+} + TFe^{2+})$) and M/F (= $Mg^{2+}/(Mn^{2+} + TFe^{2+})$ values of 67.22–68.34 and 0.87–0.92, respectively.

Table 1. Major and trace element compositions of gabbro.

Sample	AKC-Ⅳ	AKC-Ⅳ	AKC-Ⅳ	AKC-Ⅳ	AKC-Ⅳ
	Y1	Y2	Y3	Y4	Y5
SiO_2	53.33	53.2	53.78	53.75	53.72
Al_2O_3	18.25	17.93	17.88	18.04	18.19
CaO	9.01	8.7	8.8	7.86	8.03

Fe_2O_3	1.81	1.56	0.99	2.17	2.03
FeO	3.64	4.06	4.28	3.13	3.31
K_2O	1.19	1.21	1.53	1.51	1.83
MgO	6.31	6.28	6.22	6.15	6.17
MnO	0.1	0.12	0.12	0.11	0.09
Na_2O	3.01	3.03	2.96	3.79	3.01
P_2O_5	0.11	0.13	0.11	0.11	0.1
TiO_2	0.7	0.8	0.67	0.7	0.74
LOI	2.41	2.71	2.36	2.38	2.44
Total	99.86	99.73	99.69	99.71	99.68
Mg#	68.12	67.22	68.22	68.34	68.18
M/F	0.91	0.87	0.91	0.92	0.92
La	13.56	13.63	13.01	13.37	13.36
Ce	32.67	32.28	30.91	32.23	32.35
Pr	4.07	3.99	3.81	3.96	3.97
Nd	16.35	16.27	15.38	15.9	16.1
Sm	3.6	3.7	3.33	3.48	3.65
Eu	1.22	1.21	1.11	1.13	1.19
Gd	3.79	3.83	3.53	3.65	3.74
Tb	0.62	0.65	0.57	0.61	0.62
Dy	3.53	3.6	3.31	3.41	3.53
Ho	0.75	0.77	0.7	0.72	0.73
Er	2.01	2.05	1.88	1.96	2.01
Tm	0.32	0.32	0.29	0.3	0.31
Yb	1.88	1.84	1.77	1.71	1.78
Lu	0.29	0.3	0.27	0.28	0.29
Hf	9.62	11.08	10.38	10.18	10.39
Nb	5.76	6.01	5.77	5.54	5.5
Ta	1.23	1.06	0.94	0.82	0.77
W	14	15.88	16.15	13.7	22.69
Tl	0.36	0.36	0.5	0.49	0.6
Pb	14.37	13.77	17.22	13.01	13.5
Bi	0.18	0.24	0.24	0.22	0.17
Th	3.46	3.73	3.22	3.45	3.82

U	2.74	2.82	2.67	2.09	2.3
Sc	6.05	6.68	4.7	5.65	7.59
Ti	4332	4775	4123	4273	4426
V	137	143.4	128.2	132.2	135.5
Cr	14.59	11.71	13.13	11.94	11.25
Mn	842	956.6	968.8	861.9	759.1
Co	31.5	32.37	27.64	30.13	30.19
Ni	46.32	40.64	38.19	46.6	44.47
Cu	20.68	17.79	20.62	24.97	19.89
Zn	70.6	73.05	66.39	68.77	75.9
Ga	16.94	17.26	16.58	16.15	16.21
As	7.97	3.48	3.6	4.33	8.68
Rb	47.45	44.43	61.91	61.21	82.87
Sr	499.5	490	490.5	459.1	506.9
Y	15.46	15.61	13.47	14.23	15.85
Zr	95.34	111.6	106.4	98.71	104.2
Cd	1.34	1.39	1.46	1.34	1.54
Sb	5.35	5.41	5.33	5.07	5.38
Cs	7.26	6.21	6.03	7.44	7.64
Ba	219.1	258.4	345.5	241.5	334.9
ΣREE	84.67	84.42	79.85	82.71	83.62
$(La/Yb)_N$	4.88	5.01	4.96	5.28	5.07
$(La/Sm)_N$	3.51	3.43	3.65	3.58	3.42
$(Gd/Yb)_N$	1.63	1.68	1.61	1.73	1.7
Eu/Eu^*	1	0.97	0.98	0.96	0.97

The gabbros contain 79.85–84.67 ppm rare-earth elements (REE) and have right-inclined chondrite-normalized REE diagram patterns (Figure 5a) with $(La/Sm)_N$, $(La/Yb)_N$, and $(Gd/Yb)_N$ values of 3.42–3.65, 4.88–5.28, and 1.61–1.73, respectively, indicating they are enriched in LREE relative to middle REE (MREE) and HREE, with weak fractionation of MREE from HREE. No Eu anomaly ($Eu/Eu^* = \delta Eu - 2Eu_N/(Sm_N + Gd_N)$, 0.96–1.00) was observed.

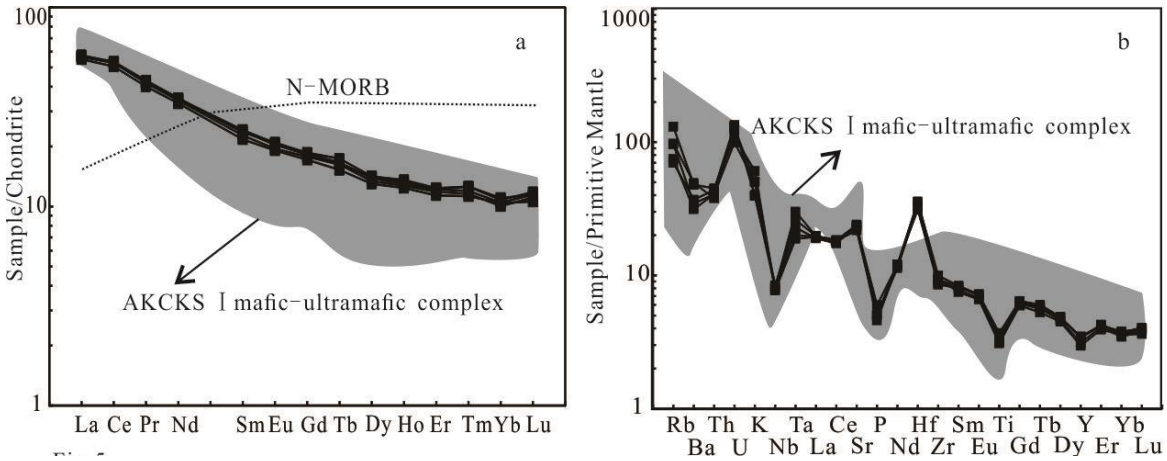

Figure 5. (**a**) Chondrite-normalized rare-earth elements (REE) patterns (after Boynton [21]) and(b) primitive-mantle-normalized spider diagrams (after McDonough and Sun [22]) for gabbros from the Akechukesai Ⅳ mafic–ultramafic complex. Gray shadow areas are from a compilation of literature data.

The gabbros on primitive-mantle-normalized multi-element variation diagrams are enriched in large-ion lithophile elements (LILE; e.g., Rb, U, and K), but negative anomalies in Nb, P, and Ti (Figure 5b). The shaded area in Figure 5b includes samples from the Akechukesai I mafic–ultramafic complex, showing the similarity of compositions of samples from these two complexes.

5.2. Zircon U–Pb Ages and Hf Isotopic Data

The results of U–Pb dating are given in Table 2. The zircons within the gabbro are primarily colorless to charcoal grey, are columnar and contain homogeneous but faintly developed zoning. They appear striped and free of inclusions under cathodoluminescence (CL) imaging and are 150–200 μm long with aspect ratios of 1:1–1.5:1. They contain 176–1617 ppm Th and 533–3421 ppm U, yielding Th/U ratios of 0.33–0.73, indicating they are of magmatic origins. A total of 17 zircons yielded a weighted-mean age of 423.9 ± 2.6 Ma (MSWD = 0.26;1σ), indicating the timing of formation of the gabbro (Figure 6).

Table 2. LA-ICP-MS U-Pb dating data of gabbro in the Akechukesai Ⅳ mafic -ultramafic complex.

No.	Content (pm)		Th/U	Isotopic Ratios						Age (Ma)					
	U	Th		$^{207}Pb/^{206}Pb$	1 σ	$^{207}Pb/^{235}U$	1 σ	$^{206}Pb/^{238}U$	1 σ	$^{207}Pb/^{206}Pb$	1 σ	$^{207}Pb/^{235}U$	1 σ	$^{206}Pb/^{238}U$	1 σ
1	2042	1491	0.73	0.0559	0.0006	0.5201	0.0085	0.0673	0.0008	447	23	425	6	420	5
2	1758	754	0.43	0.0558	0.0012	0.5190	0.0134	0.0674	0.0013	445	48	424	9	421	8
3	3421	1566	0.46	0.0559	0.0005	0.5219	0.0084	0.0674	0.0009	450	21	426	6	421	5
4	1075	456	0.42	0.0554	0.0006	0.5173	0.0081	0.0676	0.0008	428	24	423	5	421	5
5	599	218	0.36	0.0571	0.0018	0.5345	0.0207	0.0676	0.0013	494	68	435	14	422	8
6	2577	1568	0.61	0.0561	0.0006	0.5259	0.0070	0.0677	0.0008	456	22	429	5	422	5
7	1951	787	0.40	0.0555	0.0010	0.5187	0.0070	0.0678	0.0007	431	39	424	5	423	4
8	2059	1313	0.64	0.0565	0.0011	0.5303	0.0164	0.0679	0.0016	471	42	432	11	423	9
9	3051	1286	0.42	0.0559	0.0018	0.5247	0.0160	0.0679	0.0011	446	73	428	11	423	7
10	1483	596	0.40	0.0561	0.0006	0.5254	0.0111	0.0679	0.0013	456	25	429	7	424	8
11	1200	733	0.61	0.0556	0.0015	0.5174	0.0119	0.0680	0.0017	436	61	423	8	424	10
12	533	176	0.33	0.0557	0.0007	0.5244	0.0069	0.0682	0.0005	440	30	428	5	425	3

13	1276	571	0.45	0.0554	0.0012	0.5207	0.0131	0.0682	0.0012	430	49	426	9	425	8
14	1617	920	0.57	0.0542	0.0008	0.5140	0.0119	0.0685	0.0015	380	31	421	8	427	9
15	2813	1440	0.51	0.0549	0.0005	0.5210	0.0080	0.0686	0.0009	407	19	426	5	428	5
16	3280	1617	0.49	0.0548	0.0008	0.5217	0.0107	0.0688	0.0010	403	34	426	7	429	6
17	1940	632	0.33	0.0553	0.0008	0.5251	0.0085	0.0689	0.0011	422	30	429	6	429	7

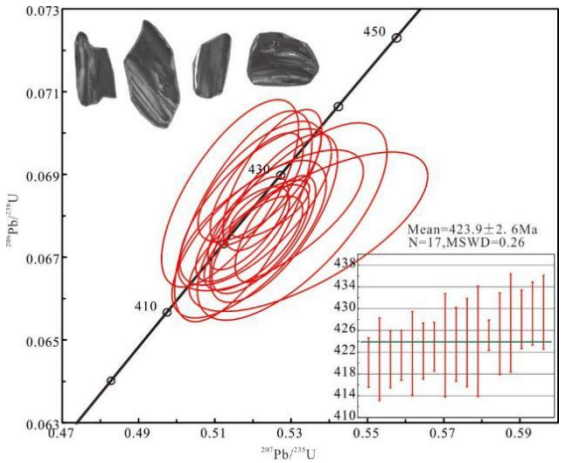

Figure 6. Zircons U–Pb concordia diagram for gabbro in Akechukesai Ⅳ mafic–ultramafic complex.

The results of *in situ* Hf isotopic analysis are given in Table 3. A total of 14 zircons yielded $\varepsilon Hf_{(t=424\ Ma)}$ values and associated T_{DM1} ages of –1.2 to –11.3 and 1535–1092 Ma, respectively. These negative εHf values contrast with the positive εHf values previously determined for the Xiarihamu and Akechukesai I mafic–ultramafic complexes (Figure 7), indicating that ancient crustal material may have been incorporated into the source.

Table 3. Zircon Lu-Hf isotopic compositions of gabbro in the Akechukesai Ⅳ mafic -ultramafic complex.

No.	Age (Ma)	$^{176}Hf/^{177}Hf$	1σ	$^{176}Lu/^{177}Hf$	1σ	$^{176}Yb/^{177}Hf$	1σ	εHf(0)	1σ	εHf(t)	1σ	T_{DM1}	T_{DM2}	fLu/Hf
1	424	0.282210	0.000014	0.002621	0.000008	0.066342	0.000314	-19.9	0.7	-11.3	0.7	1535	1907	-0.92
2	424	0.282483	0.000015	0.001150	0.000004	0.029024	0.000076	-10.2	0.7	-1.2	0.8	1092	1352	-0.97
3	424	0.282232	0.000015	0.002144	0.000017	0.056160	0.000437	-19.1	0.7	-10.4	0.8	1483	1856	-0.94
4	424	0.282436	0.000014	0.000952	0.000022	0.023045	0.000871	-11.9	0.7	-2.8	0.7	1152	1441	-0.97
5	424	0.282320	0.000013	0.002143	0.000005	0.054055	0.000192	-16.0	0.7	-7.3	0.7	1357	1686	-0.94
6	424	0.282459	0.000013	0.001239	0.000002	0.031064	0.000132	-11.1	0.7	-2.1	0.7	1128	1400	-0.96
7	424	0.282414	0.000016	0.001506	0.000004	0.041224	0.000164	-12.7	0.8	-3.8	0.8	1200	1492	-0.95
8	424	0.282434	0.000015	0.000911	0.000006	0.022934	0.000133	-11.9	0.7	-2.9	0.8	1153	1443	-0.97
9	424	0.282288	0.000016	0.001783	0.000015	0.047849	0.000497	-17.1	0.8	-8.3	0.8	1389	1742	-0.95
10	424	0.282448	0.000016	0.001339	0.000004	0.031726	0.000139	-11.4	0.8	-2.5	0.8	1146	1423	-0.96
11	424	0.282234	0.000015	0.002405	0.000006	0.061395	0.000179	-19.0	0.7	-10.4	0.8	1491	1856	-0.93
12	424	0.282371	0.000015	0.001785	0.000006	0.046687	0.000179	-14.2	0.7	-5.4	0.8	1271	1580	-0.95
13	424	0.282239	0.000015	0.002301	0.000006	0.060993	0.000179	-18.9	0.7	-10.2	0.8	1480	1845	-0.93
14	424	0.282313	0.000015	0.002226	0.000006	0.055819	0.000179	-16.2	0.7	-7.5	0.8	1370	1700	-0.93

5.3. Sulfur and Lead Isotopic Data for Sulfides

S isotopic analyses of four Akechukesai pyrite samples from vein-like mineralization yielded $\delta^{34}S$ values of 13.1‰–13.4‰, whereas five disseminated (containing pyrite and pyrrhotite) samples yielded $\delta^{34}S$ values of 5.0‰–8.5‰ (Figure 8; Table 4). Nine Akechukesai ore samples (contain pyrite and pyrrhotite) yielded $^{206}Pb/^{204}Pb$ values of 17.323–18.472, $^{207}Pb/^{204}Pb$ values of 15.422–15.626, and $^{208}Pb/^{204}Pb$ values of 37.610–38.327 (Figure 9; Table 5).

Table 4. S isotopic composition of the sulfides from the No.Ⅳ mafic -ultramafic complex.

Sample no.	Location	Sample	$\delta^{34}S$
AKC-S1	Vein-like ore	Pyrite	13.1
AKC-S2	Vein-like ore	Pyrite	13.4
AKC-S3	Vein-like ore	Pyrite	13.2
AKC-S4	Vein-like ore	Pyrite	13.4
AKC-S5	Disseminated ore	Pyrite	5.0
AKC-S6	Disseminated ore	Pyrrhotite	8.5
AKC-S7	Disseminated ore	Pyrite	7.5
AKC-S8	Disseminated ore	Pyrite	7.2
AKC-S9	Disseminated ore	Pyrite	7.5

Table 5. Pb isotopic composition of the sulfides from the No.Ⅳ mafic -ultramafic complex.

Sample no.	Location	Sample	$^{208}Pb/^{204}Pb$	$^{207}Pb/^{204}Pb$	$^{206}Pb/^{204}Pb$
AKC-Pb1	Vein-like ore	Pyrite	38.116	15.544	18.272
AKC-Pb2	Vein-like ore	Pyrite	38.233	15.591	18.276
AKC-Pb3	Vein-like ore	Pyrite	38.272	15.626	18.447
AKC-Pb4	Vein-like ore	Pyrite	38.327	15.622	18.472
AKC-Pb5	Disseminated ore	Pyrite	38.147	15.557	18.254
AKC-Pb6	Disseminated ore	Pyrrhotite	38.119	15.551	18.247
AKC-Pb7	Disseminated ore	Pyrite	38.227	15.567	18.284
AKC-Pb8	Disseminated ore	Pyrite	38.021	15.529	18.019
AKC-Pb9	Disseminated ore	Pyrite	37.610	15.422	17.323

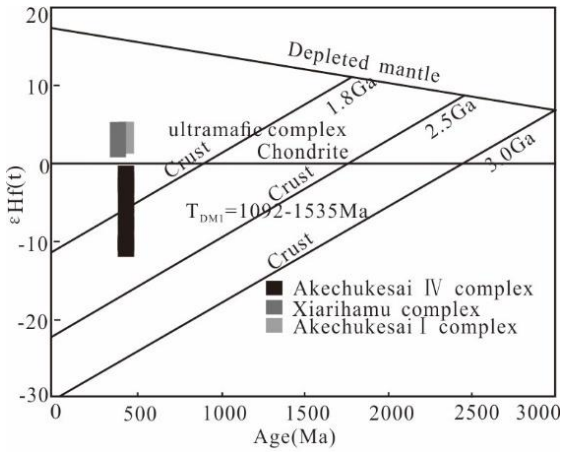

Figure 7. $\varepsilon_{Hf}(t)$ versus time (Ma) diagram for gabbro in Akechukesai Ⅳ mafic–ultramafic complex. Data sources for 1.8Ga, 2.5 Ga, and 3.0Ga lines are from Wu et al. [23]. Gray shadow areas are from Li et al. [6] and a compilation of literature data.

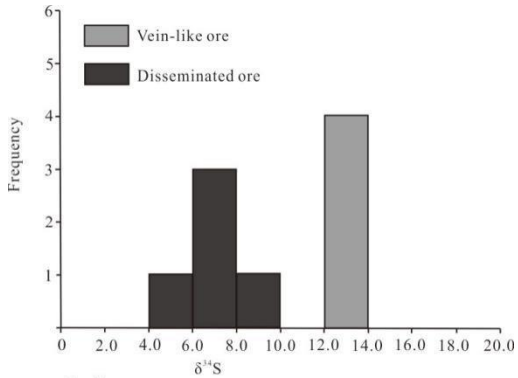

Figure 8. Histogram of S isotopic composition of sulfides from vein-like ore and disseminated ore.

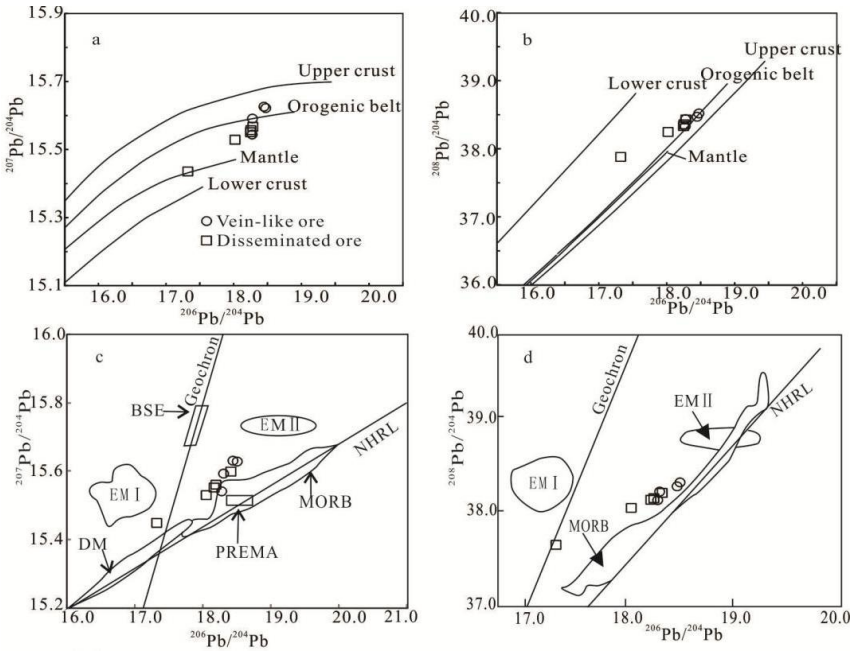

Figure 9. Diagrams of $^{206}Pb/^{204}Pb$, -$^{207}Pb/^{204}Pb$, and $^{206}Pb/^{204}Pb$ -$^{207}Pb/^{204}Pb$ of the sulfides from Akechukesai Ⅳ mafic–ultramafic complex. EM Ⅰ: enriched mantle Ⅰ; EM Ⅱ: enriched mantle Ⅱ; MORB: mid-ocean ridge basalt. Data sources: Zart and Doe [24], Allegre et al. [25], Zindler and Hart [26].

6. Discussion

6.1. Crustal and Source Contamination

Fieldwork in the study area identified an unusual lithology located at the contact between pyroxenite and marble units. This lithology is here termed contaminated rock (Figure 3e), and appears to have formed during reactions between calcium-rich marble and mantle-derived magma. The geochemistry of the gabbros in the study area also provide evidence of assimilation of crustal material, as the variations in the ratios of elements with similar distribution coefficients in the gabbros cannot be explained by partial melting and fractional crystallization alone. As such, these elemental ratios are likely to reflect crustal contamination [27]. The mantle has a uniform Ce/Pb ratio of 25 ± 5 compared to typical crustal material, which has Ce/Pb ratios < 15 [28]. The samples from the Akechukesai Ⅳ mafic–ultramafic complex have Ce/Pb ratios of 1.80–2.48, much lower than the value expected for the mantle and similar to typical crustal compositions, indicating that crustal contamination occurred.

Low Ce/Pb ratios in continental crust are usually thought to be the result of Pb enrichment during arc magmas [29], potentially by preferential extraction of Pb from subducted oceanic crustal material and the transfer of this Pb into the mantle wedge via a fluid phase generated during slab dehydration [30]. In addition, the samples from the Akechukesai Ⅳ complex have Nb/U ratios of 2.10–2.65, much lower than those of oceanic basalts (~50; [21]), bulk silicate Earth (~32; [21]), and continental upper crust (~9; [31]), but similar to arc volcanic rocks (0.3–9.0; [32]). If intrusions were generated only by contamination of the mantle-derived end-member by continental crust, the ratios of Nb/U should be intermediate between the mantle-derived end-member and continental crust. This also suggests that the primitive magma of these intrusions was originated from a metasomatized mantle source [33]. Nb/Ta ratios are ~5, different from the range of primitive mantle (17.5 ± 2; [34]) and Zr/Hf ratios (~10) deviate from the values of crust and chondrites (33–40; [35]), implying the effect of mantle metasomatic processes or fractionation of accessory mineral phases [36].

A Ba/Th versus Th (ppm) diagram can be used to identify the agent involved in the metasomatism of magma sources [37]. High Ba/Th ratios and low Th concentrations generally indicate fluid metasomatism. The samples from the Akechukesai Ⅳ mafic–ultramafic complex have high Ba/Th ratios but contain low concentrations of Th (Figure 10a), tend to be consistent with the trend of fluid metasomatism, suggesting that they record fluid metasomatism [37]. Low Th/Yb ratios commonly record fluid-related metasomatism. These samples also have relatively low Th/Yb and Ba/La values (Figure 10b), again suggesting the involvement of fluid metasomatism in their genesis [37]. Métrich et al. [38] suggested that sulfur was one of the most mobile elements to be transferred by fluids from subducted slabs to mantle wedges, as evidenced by research of a close association between S and H_2O-rich fluid undertaken on Batan Island. This reflects the fact that fluid metasomatism can dissolve and transfer soluble elements from subducted slab (Mclnnes et al. [39]). The partitioning of sulfur between different S-bearing phases during mantle melting generates a strongly heterogeneous distribution of bulk sulfur concentrations in the resultant melt as well as variations in the ^{34}S composition of the metasomatized mantle source [38].

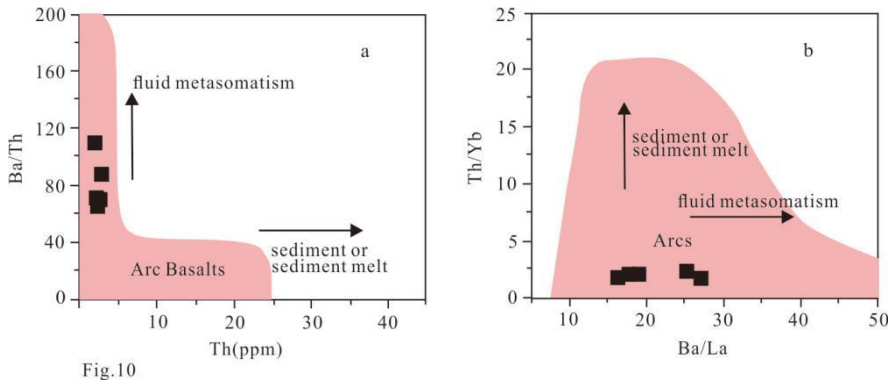

Fig.10

Figure 10. (**a**) Plot of Ba/Th vs. Th (ppm), the pink area represents the arc volcanic rocks worldwide (Kirchenbaur et al. [37] and references therein). (**b**) Th/Yb vs. Ba/La diagram, the pink area represents the oceanic arc volcanic rocks (Kirchenbaur et al. [37] and references therein).

Addition of S is often linked to the generation of magmatic sulphide mineralization as the addition of significant amounts of S may be more conducive to sulfur saturation of the magma [7]. The Akechukesai Ⅳ mafic–ultramafic complex has $\delta^{34}S$ values (5.0‰–13.4‰) that are higher than the expected value for the mantle (0‰ ± 2‰), suggesting the complex contains additional S, most likely derived from subducted oceanic crustal material. The vein-like and disseminated sulphides have significantly different $\delta^{34}S$ values, suggesting that the vein-like sulphides contain more sulfur. However, the two ore types have similar Pb isotopic compositions, suggesting they contain Pb derived from the same source. The disseminated and vein-like ores plot between orogenic belt and mantle Pb sources in Figure 9a, however, two vein-like ore samples plot between orogenic belt and upper crustal sources. The two ore types plot between orogenic belt and mantle sources in Figure 9b. Nevertheless, two disseminated samples plot between orogenic belt and lower crustal sources. This suggests that most Pb in these samples was derived from the mantle, with the crustal Pb present added as a result of orogenic processes.

6.2. Mantle Source Affinities

The presence of Nb–Ta anomalies within primitive-mantle-normalized multi-element variation diagrams can provide evidence of source characteristics [31]. Samples of the Akechukesai Ⅳ mafic–ultramafic complex have negative Nb and Ta anomalies (Figure 5b) relative to both OIB and MORB (positive Nb and Ta anomalies) that suggests the magmas that formed this complex were not derived from primary OIB or MORB sources [40].

In addition, these samples have chondrite-normalized REE patterns that are different from those of N-MORB (Figure 7a). The Hf model ages (T_{DM}) of zircons may represent the time at which they detached from depleted mantle, if the magma source has been unmodified, the crystallization time of the zircons ought to be approximately equal to the model ages. The Akechukesai IV intrusions have Hf model ages (T_{DM1} = 1535–1092 Ma) older than their crystallization ages (t = 424Ma). Compared to the Hf model ages (T_{DM1} = 610–875 Ma) of the Xiarihamu intrusions, the older Hf model ages (T_{DM1} = 1535–1092 Ma) of zircons from Akechukesai IV intrusions than their crystallization ages (t = 424Ma) may indicate that the magma source had experienced high levels of enrichment [7]. The Akechukesai IV mafic–ultramafic samples plot in the arc volcanic field on a Ce versus Ce/Pb diagram (Figure 11a) and in the E-MORB field on a Nb/Yb versus Zr/Yb diagram (Figure 11b), whereas Zr/Hf is ~10, significantly different from an E-MORB source(~43; [41,42])，similar to the range of depleted mantle peridotite (~10;[43]). However, these samples plot near the MORB area of $^{207}Pb/^{204}Pb$ versus $^{206}Pb/^{204}Pb$ and $^{208}Pb/^{204}Pb$ versus $^{206}Pb/^{204}Pb$ diagrams (Figure 9c, d), suggesting their magma source has a MORB affinity. These samples also have Zr/Nb ratios of 16.56–18.96 and Sm/Nd ratios of 0.22–0.23, both of which are in the MORB range of compositions (10–60, Davidson, [44]; average 0.32, Anderson, [45], respectively). This indicates that the magma source was most likely dominated by MORB components.

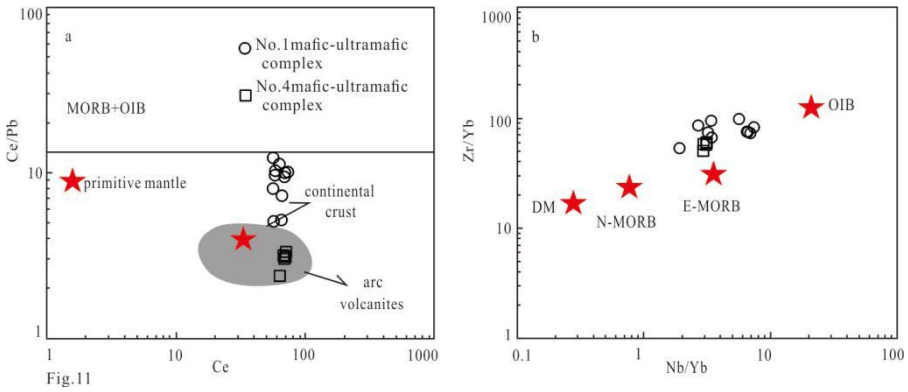

Figure 11. (**a**) Ce/Pb vs. Ce; (**b**) Zr/Yb vs. Nb/Yb plots of the Akechukesai Ⅳ mafic–ultramafic complex. Primitive mantle, DM, mid-ocean ridge basalt (MORB) and OIB from Hofmann [40], Schmidberger and Hegner [46], Harms et al. [47], Taylor and McLennan [48], Pearce et al. [49], Fitton et al. [50].

Previous research indicates that magmatic rocks generated in post-collisional extensional settings (see section 6.3) may also have the geochemical characteristics of magmas developed in island arc or active continental margin settings (Aldanmaz et al., [51]). This indicates that magma sources can retain characteristics derived from previously subducted oceanic crust, including Nb, P, and Ti depletions and enrichment in the LILE (Rb, U, and K). This has been confirmed by previous research within the EKOB on the Xiarihamu complexes by Peng et al. [7], and on the Weibao volcanic rocks by Zhong et al. [52]. The fact that the Akechukesai complex formed in a post-collisional setting (see section 6.3) suggests that it may have inherited characteristics from earlier subduction in this area, as is the case for the Xiarihamu complexes and the Weibao volcanics. This would suggest that the low $\varepsilon Hf_{(t)}$ values of the gabbros in the study area reflect subduction-related metasomatism in a similar fashion to the Xiarihamu mafic–ultramafic complexes ($\varepsilon Hf_{(t)}$ = 4–10; T_{DM1} = 610-875Ma) and the Weibao volcanic rocks ($\varepsilon Hf_{(t)}$ = –2.6 to +7.5). Lower negative values indicate that ancient crustal composition may have also been incorporated. Couzinié et al. [53] and Franciosi et al. [54] also determined that post-collisional mafic magmatism in the Variscan French Massif Central and proposed a hybrid source containing subducted components and depleted-mantle material. This is also the case for the Xiarihamu mafic–ultramafic complexes and the Weibao volcanic rocks (Peng et al., [7]; Zhong et al., [52]). The next logical step in furthering our understanding of the evolution of the Akechukesai complex would be to quantify the relative contributions of these two end-members.

Previous research has determined that garnet and spinel have different REE partition coefficients that can be used to identify whether magmas are derived from garnet- or spinel-bearing mantle material [55]. The Dy/Yb ratios of melts originating from mantle material within the spinel stability field are generally < 1.5, whereas melts derived from garnet-bearing mantle material generally have Dy/Yb ratios > 2.5 (Yang et al. [56]). In addition, melts with $(Dy/Yb)_N$ ratios < 1.06 are indicative of a magma source that contains spinel (Blundy et al. [57]). The samples from the study area have Dy/Yb ratios of 1.9–2.0 and $(Dy/Yb)_N$ ratios of 1.2–1.3, indicating they were derived from mantle material containing both garnet and spinel.

Plotting the samples from the study area on a La/Yb versus Yb diagram can provide information on source mineralogy and the degree of partial melting during magma genesis. The proportions of minerals used in this melting model are from McKenzie and O'Nions [58] and Rollinson [59]. Two curves are plotted in Figure 12 to enable the characterization of the mineralogy of the mantle source for the Akechukesai IV mafic–ultramafic complex. The samples from the complex plot between curves reflecting a mix of 5% melting of garnet lherzolite combined with 5% melting of spinel lherzolite and 10% melting of the same combination of the two lithologies. This indicates that the magmas that formed the complex derived from variable degrees of partial melting of mantle material located within both the spinel and garnet stability fields.

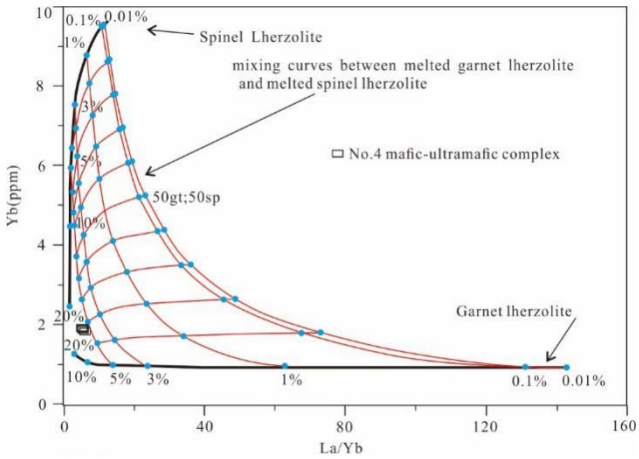

Figure 12. Plot of Yb vs. La/Yb for the Akechukesai Ⅳ mafic–ultramafic complex. Non-modal batch melting curves were calculated by using partition coefficients from McKenzie and O'Nions [58], Rollinson [59] and Keskin [60].

6.3. Geodynamic Implications

Previous research indicates that magmatic rocks generated in post-collisional extensional settings may also have the geochemical characteristics of magmas developed in island arc or active continental margin settings (Aldanmaz et al., [51]). In the EKOB, the youngest magmatism associated with early Paleozoic subduction event has been identified as 436Ma [61]. Peng et al. [7] have considered that continent collision ceased at 430Ma. Zircon U–Pb dating indicates that the Akechukesai IV mafic–ultramafic complex formed at 423.9 ± 2.6 Ma, coeval with the Akechukesai I mafic–ultramafic complex, which formed in a post-collisional environment (422 ± 10 Ma; unpublished data). Some samples from the Akechukesai IV mafic–ultramafic complex contain biotite and amphibole, indicating that the primitive magma that formed the complex was hydrous. This hydrous magma could have formed by decompression- related melting of a hydrous region of the mantle (Gao et al. [62]).These evidences indicate that the Akechukesai IV mafic–ultramafic complex may also be generated in a post-collisional environment.

Some of the mafic–ultramafic complexes and A-type granitoids in the EKOB have similar ages, as exemplified by the Xiarihamu I mafic–ultramafic complex (423 ± 1 Ma; Wang et al. [63]), the Xiarihamu II mafic–ultramafic complex (424 ± 1 Ma; Peng et al. [7]), and the Baiganhu A-type moyite and monzonitic granites (ages of 422 ± 3 and 421 ± 3.7 Ma, respectively; Li et al. [64]). The Wulonggou A2-type granite, which formed at 426–424 Ma, represents the earliest evidence for a post-orogenic tectonic setting in this area (Xin et al. [9]). The presence of these coeval middle Silurian mafic–ultramafic complexes and A-type granites provide evidence of formation in a post-collisional tectonic environment.

The EKOB experienced two stages of post-collisional mantle-derived magmatism during the middle Silurian and Late Triassic. The mineralized and prospective mafic–ultramafic complexes discovered in the EKOB to date all formed during the middle Silurian, namely the Xiarihamu, Akechukesai, Shitoukengde, and Langmuri mafic–ultramafic complexes. Although some Late Triassic mafic–ultramafic complexes have been identified in this area (e.g., the Kaimuqi and Xiaojianshan complexes), these complexes appear to be unmineralized. As such, research has focused on the middle Silurian mafic–ultramafic complexes in this area. Among these, the Xiarihamu complexes, which host a super-large Cu–Ni deposit, are primarily studied in this area, and have characteristics that are representative of the other mafic–ultramafic complexes formed at this time. Combined with the regional tectonic evolution, Wang et al. [63] and Peng et al. [7] suggest that the Xiarihamu mafic–ultramafic complexes formed in a post-collisional tectonic setting associated with closure of the proto-Tethyan Ocean. The dehydration of the subducted slab generated a water-rich fluid phase that migrated into and subsequently metasomatized (and transported S into) the overlying mantle wedge. The thickness of this oceanic plateau material (up to 36 km) impeded normal

subduction, potentially causing break-off of the subducted slab [12]. This would allow hot asthenospheric mantle material to ascend through the resulting slab window, causing shallower decompression melting. This slab break-off model is consistent with the linear distribution of mafic–ultramafic complexes along the middle Kunlun fault.

7. Conclusions

1. The Akechukesai IV mafic–ultramafic complex was formed at 423.9 ± 2.6 Ma and it was just one of the mafic–ultramafic complexes emplaced in the middle Silurian within the post-collisional tectonic framework of the EKOB.

2. Hf–S–Pb isotopes and geochemical data indicate that primitive magma has a MORB affinity and is derived from a mantle source that is metasomatized by subduction-related fluids. The older T_{DM1} ages than crystallization ages indicate that the original source experienced some enrichment. The magma source is composed of a mix between 5% melted garnet lherzolite—5% spinel lherzolite and 10% melted garnet lherzolite—and 10% spinel lherzolite.

3. Addition of high amounts of sulfur may have had a significant role in driving S saturation, leading to the precipitation of sulfide minerals.

Author Contributions: Conceptualization, J.-M.Y. and F.-Y.S.; Methodology, Y.-S.Z.; Software, Y.Q.; Validation, F.-Y.S., J.-M.Y.; Formal Analysis, Z.-P.Y.; Investigation, J.-M.Y.; Resources, F.-Y.S.; Data Curation, J.-M.Y. and L.L.; Writing—Original Draft Preparation, J.-M.Y.; Writing—Review & Editing, F.-Y.S.; Visualization, J.-M.Y.; Supervision, Y.Q.; Project Administration, F.-Y.S.; Funding Acquisition, F.-Y.S.

Funding: This research was financially supported by National Natural Science Foundation of China (No.41272093).

Acknowledges: We thank the staff of Qinghai Kanghua Minging limited company for field investigation and the staff of laboratory for the analyses.

Conflicts of Interest: The authors declare no conflict of interest.

References

1. Meng, F.C.; Cui, M.H.; Wu, X.K.; Ren Y.F. Heishan mafic–ultramafic rocks in the Qimantag area of Eastern Kunlun, NW China: Remnants of an early Paleozoic incipient island arc. *Gondwana Res.* **2015**, 27, 745–759.
2. Yuan, C.; Zhou, M.F.; Sun, M.; Zhao, Y.J.; Wilde, S.; Long, X.P.; Yan, D.P. Triassic granitoids in the eastern Songpan Ganzi Fold Belt, SW China, Magmatic response to geodynamics of the deep Lithosphere. *Earth Planet. Sci. Lett.* **2010**, *290*, 481–491.
3. Xu, Z.Q.; Yang, J.S.; Li, H.B.; Zhang, J.X.; Wu, C.L. *Terrane Amalgamation, Collision and Uplift in the Qinghai-Tibet Plateau*; Geological Publishing House: Beijing, China, 2007, pp. 1–458.
4. Li, X.W.; Huang, X.F.; Luo, M.F.; Dong, G.C.; Mo, X.X. Petrogenesis and geodynamic implications of the Mid-Triassic lavas from East Kunlun, northern Tibetan Plateau. *J. Asian Earth Sci.* **2015**, *105*, 32–47.
5. Xiong, F.H.; Ma, C.Q.; Wu, L.; Jiang, H.A.; Liu, B. Geochemistry, zircon U–Pb ages and Sr–Nd–Hf isotopes of an Ordovician appinitic pluton in the East Kunlun orogen: New evidence for Proto-Tethyan subduction. *J. Asian Earth Sci.* **2015**, *111*, 681–697.
6. Li, C.S.; Zhang, Z.W.; Li, W.Y.; Wang, Y.L.; Sun, T.; Ripley, E.D. Geochronology, petrology and Hf–S isotope geochemistry of the newly-discovered Xiarihamu magmatic Ni–Cu sulfide deposit in the Qinghai–Tibet plateau, western China. *Lithos* **2015**, *216–217*,224–240.
7. Peng, B.; Sun, F.Y.; Li, B.L.; Wang, G.; Li, S.J.; Zhao, T.F.; Li, L.; Zhi, Y.B. The geochemistry and geochronology of the Xiarihamu II mafic-ultramafic complex, Eastern Kunlun, Qinghai Province, China: Implications for the genesis of magmatic Ni-Cu sulfide deposits. *Ore Geol. Rev.* **2016**, *73*, 13–28.

8. Shao, F.L.; Niu, Y.L.; Liu, Y.; Chen, S.; Kong, J.J.; Duan, M. Petrogenesis of Triassic granitoids in the East Kunlun Orogenic Belt, northern Tibetan Plateau and their tectonic implications. *Lithos* **2017**, *282–283*, 33–44.
9. Xin, W.; Sun, F.Y.; Li, L.; Yan, J.M.; Zhang, Y.T.; Wang, Y.C.; Shen, T.S.; Yang, Y.J. The Wulonggou metaluminous A2-type granites in the Eastern Kunlun Orogenic Belt, NW China: Rejuvenation of subduction-related felsic crust and implications for post-collision extension. *Lithos* **2018**, *312–313*, 108–127.
10. Jiang, C.Y.; Ling, J.; Zhou, W.; Du, W.; Wang, Z.; Fan, Y.; Song, Y.; Song, Z. Petrogenesis of the Xiarihamu Nibearing layered mafic-ultramafic intrusion, East Kunlun: Implications for its extensional island arc environment. *Acta Petrol. Sin*. **2015**, *31*, 1117–1136.
11. Song, X.Y.; Yi, J.N.; Chen, L.M.; She, Y.W.; Liu, C.Z.; Dang, X.Y.; Yang, Q.A.; Wu, S.K. The Giant Xiarihamu Ni-Co sulfide deposit in the East Kunlun Orogenic Belt, Northern Tibet Plateau.China. *Econ. Geol*. **2016**, *111*, 29–55.
12. Sun, F.Y.; Chen, G.H.; Chi, Q.G. Report of metallogenic regularity and prospecting direction comprehensive study in Xinjiang–East Kunlun metallogenic belt. 2003 (in Chinese).
13. Wang, G.C.; Wang, Q.H.; Ping, J.; Zhu, Y.H. Zircon SHRIMP ages of Precambrian metamorphic basement rocks and their tectonic significance in the Eastern Kunlun Mountains, Qinghai province, China. *Earth Sci. Front.* **2004**, *11*, 481–490.（In Chinese）
14. Yuan, H.L.; Gao, S.; Liu, X.M.; Li, H.M.; Gunther, D.; Wu, F.Y. Accurate U–Pb age and trace element determinations of zircon by laser ablation—inductively coupled plasma mass spectrometry. *Geostand. Newslett*. **200**4, *28*, 353–370.
15. Andersen, T. Correction of common lead in U–Pb analyses that do not report ^{204}Pb Chem. *Geol*, **2002**, *192*, 59–79.
16. Liu, Y.S.; Hu, Z.C.; Gao, S.; Günther, D.; Xu, J.; Gao, C.G.; Chen, H.H. In situ analysis of major and trace elements of anhydrous minerals by LA-ICP-MS without applying an internal standard Chem. *Geol*. **2008**, *257*, 34–43.
17. Ludwig, K.R. *User's Manual for Isoplot/Ex v30, a Geochronology Toolkit for Microsoft Excel.* Berkeley Geochronological Center Special Publications: Berkeley, CA, USA; 2003, *4*, pp. 25–31.
18. Blichert-Toft, J.; Albarède, F. The Lu–Hf geochemistry of chondrites and the evolution of the mantle–crust system. *Earth Planet. Sci. Lett.* **1997**, *148*, 243–258.
19. Wu, F.Y.; Yang, Y.H.; Xie, L.W.; Yang, J.H.; Xu, P. Hf isotopic compositions of the standard zircons and baddeleyites used in U-Pb geochronology. *Chem. Geology* **2006**, *234*, 105–126.
20. Guo, C.L.; Chen, Y.C.; Zeng, Z.L.; Lou, F.S. Petrogenesis of the Xihuashan granites in southeastern China: Constraints from geochemistry and in-situ analysis of zircon U-Pb-Hf-O isotopes. *Lithos* **2012**, *148*, 209–227.
21. Boynton, W.V. Geochemistry of the rare earth elements: Meteorites studies. In *Rare Earth Element Geochemistry*; Henderson, P. (Ed.); Elservier: Amsterdam, The Netherlands, **1984**, 63–114.
22. McDonough, W.F.; Sun, S.S. The composition of the earth. *Chemical Geology* **1995**, *120*, 223–253.
23. Wu, F.Y.; Li, X.H.; Zheng, Y.F.; Gao, S. Lu-Hf isotopic systematics and their applications in petrology. *Acta Petrological Sinica* **2007**, *23*, 185–220.
24. Zartman, R. E.; Doe, B. R. Plumbo tectonics- the model. *Tectonophysics* **1981**, *75*, 135–162.
25. Jochum, K.P.; Seufert, H.M.; Spettel, B.; Palme, H. The solar-system abundances of Nb, Ta and Y, and the relative abundances of refractory lithophile elements in differentiated planetary bodies. *Geochim. Cosmochim. Acta*. **1986**, *50*, 1173–1183.
26. Zindler, A.; Hart, S.R. Chemical geodynamics: Annu al Rev. *Earth Planet Sci.* **1986**, *14*, 493–571.
27. Tang, D.M.; Qin, K.Z.; Sun, H.; Su, B.X.; Xiao, Q.H. The role of crustal contamination in the formation of Ni-Cu sulfide deposits in Eastern Tianshan, Xinjiang, Northwest China: Evidence from trace element geochemistry, Re-Os, Sr-Nd, zircon Hf-O, and sulfur isotopes. *J. Asian Earth Sci.* **2012**, *49*, 145–160.
28. Hofmann, A.W. Chemical differentiation of the earth: the relationship between mantle, continental crust, and oceanic crust. *Earth Planet. Sci. Lett* **1988**, *90*, 297–314.
29. Brenan, J.M.; Shaw, H.F.; Ryerson, F.J. Experimental evidence for the origin of lead enrichment

in convergent-margin magmas. *Nature* **1995**, *378*, 54–56.
30. Miller, D.M.; Goldstein, S.L.; Langmuir, C.H. Cerium/lead and lead isotope ratios in arc magmas and the enrichment of lead in the continents. *Nature* **1994**, *368*, 514–520.
31. Rudnick, R.; Fountain, D. Nature and composition of the continental crust: A lower crustal perspective. *Rev. Geophys.* **1995**, *33*, 267–309.
32. Chung, S.L.; Wang, K.L.; Crawford, A.J.; Kamenetsky, V.S.; Chen, C.H.; Lan, C.Y.; Chen, C.H. High-Mg potassic rocks from Taiwan: implications for the genesis of orogenic potassic lavas. *Lithos* **2001**, *59*, 153–170.
33. Deng, Y.F.; Song, X.Y.; Hollings, P.; Zhou, T.F.; Yuan, F.; Chen, L.M.; Zhang, D.Y. Role of asthenosphere and lithosphere in the genesis of the Early Permian Huangshan mafic–ultramafic intrusion in the Northern Tianshan, NW China. *Lithos* **2015**, *227*, 241–254.
34. Green, T.H. Significance of Nb/Ta as an indicator of geochemical processes in the crust-mantle system. *Chem. Geol*. **1995**, *120*, 347–359.
35. Dostal,J.; Chatterjee, A.K. Contrasting behavior of Nb/Ta and Zr/Hf ratios in a peraluminous granitic pluton (Nova Scotia,Canada). *Chem. Geol*. **2000**, *163*, 207–218.
36. Jochum, K.P.; Seufert, H.M.; Thirlwall, M.F. High-sensitivity Nb analyses by spark-source mass spectrometry (SSMS) and calibration of XRF Nb and Zr. *Chem. Geol*. **1990**, *81*, 1–16.
37. Kirchenbaur, M.; Münker, C.; Schuth, S.; Garbe-Schönberg, D.; Marchev, P.; Tectonomagmatic constraints on the sources of Eastern Mediterranean K-rich lavas. *J. Petrol* **2012**, *53*, 27–65.
38. Métrich, N.; Schiano, P.; Clocchiatti, R.; Maury, R, C. Transfer of sulfur in subduction settings: an example from Batan Island (Luzon volcanic arc, Philippines). *Earth Planet. Sci. Lett.***1999**, *167*, 1–14.
39. Mclnnes, B.I.A.; Grégoire, J.; Binns, R.A.; Herzig, P.M.; Hannington, M.D. Hydrous metasomatism of oceanic sub-arc mantle, Lihir, Papua New Guinea: petrology and geochemistry of fluid-metasomatised mantle wedge xenoliths. *Earth Planet. Sci. Lett.* **2001**, *188*, 169–183.
40. Hofmann, A.W.; Jochum, K.P.; Seufert, M.; White, W.M. Nb and Pb in oceanic basalts: New constraints on mantle evolution. *Earth Planet. Sci. Lett*. **1986**, *79*, 33–45.
41. 41 Gale, A.; Dalton, C.A.; Langmuir, C.H.; Su, Y.; Schilling, J.G. The mean composition of ocean ridge basalts. *Geochem. Geophys. Geosyst*. **2013**, *14*, 489–518
42. Mazzeo, F.C.; D'Antonio, M.; Arienzo, I.; Aulinas, M.; Di Renzo, V.; Gimeno, D. Subduction-related enrichment of the Neapolitan volcanoes (Southern Italy) mantle source: New constraints on the characteristics of the slabderived components. *Chemical Geol.* **2014**, *386*, 165–183.
43. Weyer, S.; Münker, C.; Mezger, K. Nb/Ta, Zr/Hf and REE in the depleted mantle: Implications for the differentiation history of the crustmantle system. *Earth Planet. Sci. Lett.* **2003**, *205*, 309–324.
44. Davidson, J.P. *Deciphering Mantle and Crustal Signatures in Subduction Zone Magmatism: Subduction Top to Bottom*; Geophysical Monograph; American Geophysical Union: Washington DC, USA; 1996, pp. 251–262.
45. Anderson, D.L. Komatites and picrites: Evidence that"plume" source is depleted. *Earth Planet. Sci. Lett.* **1994**, *128*, 303–311.
46. Schmidberger, S.S.; Hegner, E. Geochemistry and isotope systematics of calcalkaline volcanic rocks from the Saar-Nahe basin (SW Germany)-implications for Late-Variscan orogenic development. *Contrib. Mineral. Petrol*. **1999**, *135*, 373–385.
47. Harms, U.; Cameron, K.L.; Simon, K.; Bratz, H. Geochemistry and petrogenesis of metabasites from the KTB ultradeep borehole, Germany. *Geol. Rundsch* **1997**, *86*, 155–166.
48. Taylor, S.R.; Mclennan, S.M. *The Continental Crust: Its Composition and Evolution*; Blackwell Publication: Oxford, UK, 1985.
49. Pearce, J.A.; Bender, J.F.; De Long, S.E.; Kidd, W.S.F.; Low, P.J.; Güner, Y.; Saroğlu, F.; Yılmaz, Y.; Moorbath, S.; Mitchell, J.G. Genesis of collision volcanism in Eastern Anatolia, Turkey. *J. Volcanol. Geotherm. Res.* **1990**, *44*, 189–229.
50. Fitton, J.G.; James, D.; Leeman, W.P. Basic magmatism associated with Late Cenozoic extension in the western United States: compositional variations in space and time. *J. Geophys. Res*. **1991**, *96*, 13693–13712.

51. Aldanmaz, E.; Pearce, J.A.; Thirlwall, M.F.; Mitchell, J.G. Petrogenetic evolution of late Cenozoic, post-collision volcanism in western Anatolia, Turkey. *J. Volcanol. Geotherm. Res.* **2000**, *102*, 67–95.
52. Zhong, S.H.; Feng, C.Y.; Seltmann, R.; Li, D.X. Middle Devonian volcanic rocks in the Weibao Cu–Pb–Zn deposit, East Kunlun Mountains, NW China: Zircon chronology and tectonic implications. *Ore Geol. Rev.* **2017**, *84*, 309–327.
53. Couzinié, S.; Laurent, O.; Moyen, J.F.; Zeh, A.; Bouilhol, P.; Villaros, A. Post-collisional magmatism: Crustal growth not identified by zircon Hf–O isotopes. *Earth Planet. Sci. Lett.* **2016**, *456*, 182–195.
54. Franciosi, L.; D'Antonio, M.; Fedele, L.; Guarino, V.; Tassinari, C.C.G.; Gennaro, R.de.; Cucciniello, C. Petrogenesis of the Solanas gabbro-granodiorite intrusion, Sàrrabus (southeastern Sardinia,Italy): Implications for Late Variscan magmatism. *Int. J. Earth Sci.* **2019**, *108*, 989–1012.
55. Thirlwall, M.F.; Upton, B.G.J; Jenkins, C. Interaction between continental lithosphere and the Iceland plume-Sr–Nd–Pb isotope geochemistry of tertiary basalts, NE Greenland. *J. Petrol*. **1994**, *35*, 839–879.
56. Yang, W.; Niu, H.; Shan, Q.; Luo, Y.; Sun, W.; Li, C.; Li, N.; Yu, X. Late Paleozoic calcalkaline to shoshonitic magmatism and its geodynamic implications, Yuximolegai area, western Tianshan, Xinjiang. *Gondwana Res* **2012**, *22*, 325–340.
57. Blundy, J.; Robinson, J.; Wood, B. Heavy REE are compatible in clinopyroxene on the spinel lherzolite solidus. *Earth Planet. Sci. Lett*. **1998**, *160*, 493–504.
58. McKenzie, D.P.; O'Nions, R.K. Partial melt distributions from inversion of rare earth element concentrations. *J. Petrol*. **1991**, *32*, 1021–1091.
59. Rollinson, H. *Using Geochemical Data: Evaluation, Presentation, Interpretation*; Longman Scientific and Technical: Singapore, 1993.
60. Keskin, M. FC-Modeler: A Microsoft® Excel© spreadsheet program for modeling Rayleigh fractionation vectors in closed magmatic systems. *Comput. Geosci*. **2002**, *28*, 919–928.
61. Liu, B.; Ma, C.Q.; Jiang, H.A.; Guo, P.; Zhang, J.Y.; Xiong, F.H. Early Paleozoic tectonic transition from ocean subduction to collisional orogeny in the Eastern Kunlun region: Evidence from Huxiaoqin mafic rocks. *Acta Petrol. Sin.* **2013**, *29*, 2093–2106 (in Chinese with English abstract).
62. Gao, J.F.; Zhou, M.F.; Lightfoot, P.C.; Wang, C.Y.; Qi, L. Origin of PGE-poor and Cu rich magmatic sulfides from the Kalatongke deposit, Xinjiang, NW China. *Economic Geology*. **2012**, *107*, 481–506.
63. Wang, G.; Sun, F.Y.; Li, B.L.; Li, S.J.; Zhao, J.W.; Ao, C.; Yang, Q.A. Zircon U–Pb geochronology and geochemistry of the mafic–ultramafic intrusion in Xiarihamu Cu–Ni deposit from East Kunlun, with implications for geodynamic setting. *Earth Sci. Front*. **2014**, *21*, 381–401 (In Chinese).
64. Li, G.C.; Feng, C.Y.; Wang, R.J.; Ma, S.C.; Li, H.M.; Zhou, A.S. SIMS zircon U–Pb age, petrochemistry and tectonic implications of granitoids in northeastern Baiganhue W–Sn Orefield, Xinjiang. *Acta Geosci. Sin*. **2012**, *33*, 216–226 (In Chinese).

© 2019 by the authors. Licensee MDPI, Basel, Switzerland. This article is an open access article distributed under the terms and conditions of the Creative Commons Attribution (CC BY) license (http://creativecommons.org/licenses/by/4.0/).